Atomistic simulations of surface reactions in ultra-high-temperature ceramics: O_2, H_2O and CO adsorption and dissociation on ZrB_2 (0001) surfaces

Yanhui Zhang[a,b], Stefano Sanvito[b]

[a]School of Materials Science and Engineering, Yanshan University, Qinhuangdao, Hebei 066004, China
[b]School of Physics and CRANN, Trinity College Dublin, Dublin 2, Dublin, Ireland

Abstract

Understanding surface reactivity is crucial in many fields, going from heterogeneous catalysis to materials oxidation and corrosion. In order to better decipher the initial stage of surface reactions of ZrB_2 exposed to the harsh environment of aerospace components, the chemical activity of both Zr- and B-terminated (0001) surfaces is predicted and compared by using state-of-the-art density functional theory. In particular the adsorption, dissociation and diffusion of O_2, CO and H_2O are extensively examined through the calculation of the surface adsorption energies and reaction pathways. We find the dissociative adsorption of O_2 dominating the reactivity of both Zr- and B-surfaces, while the dissociation of H_2O and CO is weakly active on Zr-terminated surfaces, and even less activated on B-terminated ones. Importantly, we discover that the reaction of O_2 and H_2O can trigger surface reconstruction at the B termination, an efficient mechanism for B removal. Our work thus provides thermodynamic and kinetic insights into the elementary reactions of the most dominant gases found in the environment typical of aerospace applications, and highlights the diverse surface reaction mechanisms when ZrB_2 exposed to O_2, CO and H_2O.

Keywords: First-principles calculation, Surface reactions, dissociation barriers, surface adsorption, ZrB_2

1. Introduction

Ultra-high-temperature ceramics (UHTCs) form a family of materials defined by an extreme temperature range of operation, which includes transition metal carbides, nitrides and diborides. UHTCs are very actively researched for extensive application in various aerospace fields (as thermal

Email address: sanvitos@tcd.ie (Stefano Sanvito[b])

protection systems in hypersonic or atmospheric reusable re-entry vehicles, propulsion components, combustion chambers, engine intakes and rocket nozzles), in energy (in nuclear fission and fusion, energy harvesting, concentrated solar power), in materials processing (as high-temperature electrodes, high-speed machining tools, molten metal containment), in microelectronics (as conductors, barrier layers, lattice-matched substrates for semiconductors), just to name a few. [1, 2, 3, 4] Typically, UHTCs are characterised by the exceptional combination of mechanical, thermal and electrical properties, coupled with melting temperatures in excess of 3000 °C. These features allow UHTCs to work in extreme environments as high-temperature and aggressive atmosphere. However, the attack of the chemical agents usually found in real-life hybrid-fuel rockets, namely O_2, H_2O and CO, still pose huge challenges to the structural integrity of many components. In fact, these induce changes in the surface chemistry, causing corrosion and facilitating rapid ageing. For this reason, a comprehensive understanding of the UHTCs surface reactivity is essential for improving their structural stability and thus ultimately the safety of UHTC-based parts.

Several experimental investigations have been conducted to unveil the primary surface reactions of various UHTCs, although most of these studies are only focused on adsorption intermediates or dissociation products. For instance, dissociative adsorption of O_2 was observed on $ZrB_2(0001)$ by using high-resolution electron energy loss spectroscopy (HREELS) [5]. Belyansky and Trenary [6] have scrutinized the surface activity of the $HfB_2(0001)$ and Hf(0001) surfaces, with the help of X-ray photo-emission spectroscopy (XPS) and RAIRS (reflection adsorption infrared spectroscopy). Molecular adsorption of CO was found on $HfB_2(0001)$, while its dissociative adsorption was observed only on Hf(0001). In addition, the adsorption of O on the 3-fold hollow site of $HfB_2(0001)$ was measured by an impact-collision ion scattering spectroscopy (ICISS) study [7]. Similar studies have been carried out for carbides as well. For instance, the oxidation process of ZrC was investigated with angle resolved photo-emission spectroscopy (ARPES) [8], which identified carbon depletion with the concomitant Zr partial oxidation in the form of ZrO_x ($1 \leq x \leq 2$). Furthermore, at an oxygen-modified ZrC(100) surface, the dissociation of H_2O into hydroxyl (OH) and atomic O species was discovered by a combination of ultraviolet photoelectron spectroscopy (UPS) and XPS measurements. [9]

As an alternative to experiments, atomistic simulations provide a powerful tool to explore surface reactions in more details. For example, by using density functional theory (DFT) calculations, Sayós et al. [10] proposed that the adsorption of atomic O on the ZrB_2 (0001) surface takes place predominantly at the hollow and B-B bridge sites. Zhou et al. [11, 12] emphasized the effects of

the valance electron concentration on the surface stability and oxygen adsorption. The theoretical study of oxidation of ZrB_2 (0001) surface from Cheng et al [13] suggested that the initial oxygen coverage has only little effect on the oxidation reaction. The similar feature was also claimed for H_2O adsorption on TiO_2 [14]. Cristol et al. [15] performed a statistical thermodynamics study of O_2, H_2 and H_2O on a bare and ZrO-modified ZrC (100) surface. They suggested that the oxygen modification activates the (100) surface, and water adsorbs strongly either as atomic O with H_2 release or into surface OH and H groups. Despite these early studies, a systematic investigation of the surface activity of UHTCs, looking on an equal footing at O_2, CO and H_2O, is still missing. This is not ideal, since the reaction kinetic and its atomic characteristics are both required to effectively guide the tailoring of UHTC materials against oxidation and corrosion.

Among the UHTC family ZrB_2 stands out because of its excellent chemical stability, high hardness and strength, great thermal-stress resistance and good electrical and thermal conductivities. [16]. In this work, we study in detail the surface activity of ZrB_2 with the most common chemical agents: O_2, H_2O and CO. These are among the most abundant chemical agents in the combustion gas of hybrid-fuel rockets. The paper is organised as follows. A brief review of the atomic models (surface slabs, adsorption sites and adsorbate geometries) and the calculation details are provided in section 2. Then, an examination of atomic adsorption of O, H, OH and C on Zr-terminated $(0001)_{Zr}$ and B-terminated $(0001)_B$ surfaces, and the related surface distortions are introduced in section 3. The adsorption and dissociation mechanism of O_2, H_2O and CO are separately presented in sections 4, 5 and 6, while a comparison of the surface reactivity for the three molecules is discussed in section 7. Finally section 8 contains the main concluding remarks. Supplementary Information (SI) complements the materials included here.

2. Methodology

2.1. Surface models

In order to investigate the ZrB_2 reactivity we construct 2×2×7 (0001) surface slabs, whose structure is reported in Fig. 1(a) and 1(b). In particular, we consider both Zr [see Fig. 1(a)] and B [see Fig. 1(b)] terminations, which are denoted respectively as $(0001)_{Zr}$ and $(0001)_B$. These are selected, since they can be easily stabilized in either a Zr- or a B-rich chemical environment, as validated both in experiments and theory [17, 18, 19]. Our surface slab models are deliberately built up with a symmetric termination so as to reduce spurious dipole effects. In general, periodic boundary conditions are applied in the x-y plane, while a vacuum region of around 26 Å is added

along the z direction (perpendicular to the surface) to avoid the artificial surface-surface interaction between the periodic replicas.

2.2. Adsorption sites

The inequivalent adsorption sites over the $(0001)_{\mathrm{Zr}}$ and $(0001)_{\mathrm{B}}$ surfaces are identified within the smallest structural unit of each surface, namely the threefold Zr-triangle and the six-member B ring depicted by the dotted lines in Figs. 1(a) and 1(b), respectively. For $(0001)_{\mathrm{Zr}}$ there are three inequivalent adsorption sites, an hollow site (**H1**), a bond bridge one (**B1**) and the atop (**A1**). Similarly, four sites are identified at the $(0001)_{\mathrm{B}}$ surface, two hollow positions (**H2** and **H3**), one bond-bridge site (**B2**) and one atop (**A2**). An additional possible adsorption site, denoted as $\mathbf{B}^*$ in Fig. 1(b), always relaxes to the **H2** position so that is deemed unstable and it is excluded from further study.

2.3. Adsorbate geometries

Besides the inequivalent adsorption sites the adsorbates can also be distinguished from each other by the way they approach the surface, namely by their adsorption geometry. Broadly speaking one can separate between the situations in which all the molecule atoms lay parallelly with the surface plane (lateral geometry, **L**), or when they are perpendicular to the surface (vertical geometry, **V**). These two situations are illustrated for H_2O in Fig. 1(c). Furthermore, for hetero-molecules like CO the adsorption geometry can be further characterised by the alignment of the molecule with respect to the crystalline axes for the **L** case and by the specific atom closest to the surface in the **V** situation. Thus, for CO we have two inequivalent lateral orientations, denoted as **L**(x) and **L**(y) in Figs. 1(d1) and 1(d2), respectively (for the Zr-terminated surface), and two inequivalent vertical ones, **V(C)** and **V(O)** [see Figs. 1(d3) and 1(d4)]. The different adsorption states **H1_L(x)**, **H1_L(y)**, **H1_V(C)** and **H1_V(O)** will be examined in detail in section 6. The adsorption energy is then simply calculated as,

$$\Delta E_{\mathrm{ads}} = E^{\mathrm{sub}} + E^{x} - E^{x/\mathrm{sub}}\,, \tag{1}$$

where, $E^{x/\mathrm{sub}}$, E^{sub} and E^{x} are, respectively, the DFT total energies of the surface slab including the x adsorbent, the clean surface and the adsorbent either in gas phase or as an isolated atom. The value of ΔE_{ads} (eV/atom) measures the reactivity of the various surface sites and the binding strength of the various adsorbate-adsorbent pairs.

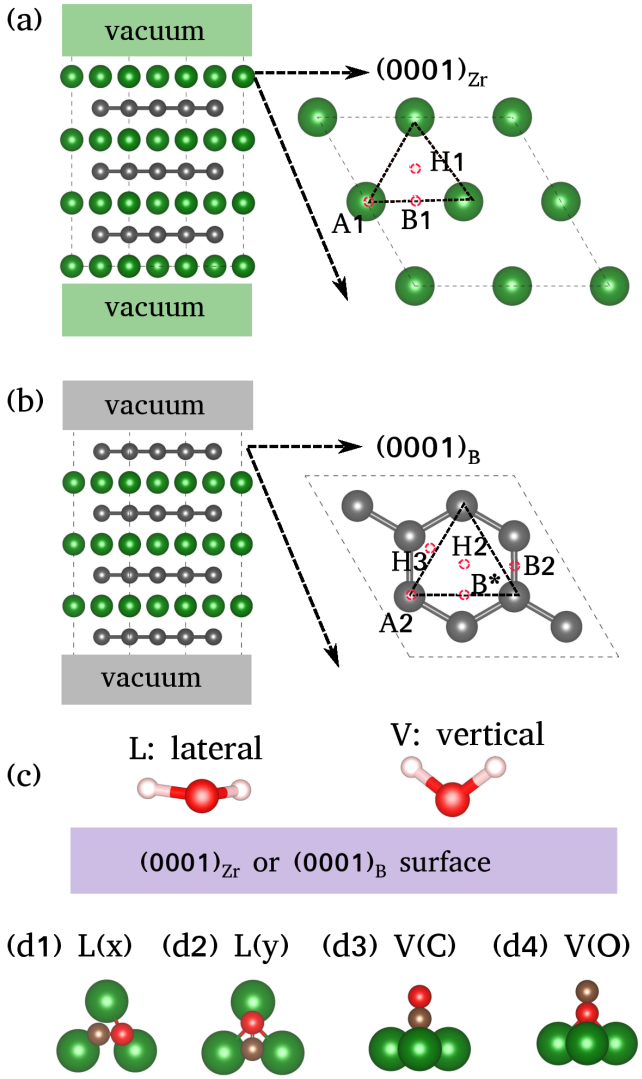

Figure 1: Surface slab models of (a) $(0001)_{Zr}$ and (b) $(0001)_{B}$ slab with side (left-hand side panels) and top (right-hand side panels) views. The inequivalent adsorption sites (hollow: **H**; bond-bridge: **B**; atop: **A**) are marked by red circles on the top views. Note that two different hollow sites (**H2** and **H3**) are found on $(0001)_{B}$, while the $\mathbf{B}^{*}$ position is unstable and relaxes into **H2**. The adsorbate geometries are labelled according to the adsorption sites, the approaching ways and the near-end species and/or alignment axis. The approaching geometry can be either lateral, **L**, or vertical, **V**. These two options are illustrated for H_2O in panel (c), and further for CO adsorbing on the hollow site of $(0001)_{Zr}$ in (d1) **H1_L(x)**, (d2) **H1_L(y)**, (d3) **H1_V(C)** and (d4) **H1_V(O)**. Colour code: Zr green; B grey; C brown; O red; H pink.

2.4. DFT calculation details

All the calculations are performed using the plane-wave basis-projector augmented-wave method (PAW) [20] as implemented in the VASP [21] code. The generalized gradient approximation (GGA) with the Perdew-Burke-Ernzerhof (PBE) [22] parametrization is adopted to evaluate the exchange and correlation energy. Recently, it has been shown that, in general, dispersion interactions strongly influence adsorption geometries and binding energies [23]. Here we include these by mean of the DFT-D2 correction [24], which has been proved adequate in the description of transition-metal diborides [19]. The calculated adsorption energies are compared to those obtained with rPBE+D2 and rPBE+D3 in Fig. S1 of the SI, showing little variations with the details of the PBE functional and the van der Waals corrections chosen. For all surface calculations the Brillouin zone is sampled by using the Monkhorst-Pack method with a k-mesh of 8×8×1. The plane-wave kinetic energy cutoff is set to 500 eV. Geometry optimization is performed until the energy and the forces are converged within 10^{-7} eV and 0.01 eV/Å, respectively, and dipole corrections [25] are applied [see the electrostatic potential profile after dipole correction in Fig. S2 of the SI]. Lastly, note that spin-polarization must be included when computing the total energy of the isolated species O, C, OH, O_2 and H, while it is not relevant for the slab calculations.

The minimum energy paths for the molecules dissociation are refined by using the nudged-elastic band (NEB) method [26, 27]. Thereafter, the transition states (TS) are located by using the climbing-image NEB algorithm with a force threshold of 0.01 eV/Å. During the relaxation of each reaction path, the adsorbent atoms on the first layer of the slab are allowed to move away from their high-energy and high-stress positions. This scheme enables us to probe the surface dissociation process, to assess whether there are kinetic bottlenecks in the surface reaction, and to monitor the accompanying distortions of the adsorbents.

3. Atomic adsorption

The fingerprint of chemisorption, namely a positive ΔE_{ads} according to Eq. (1), is observed for all the chemical species investigated, namely for O, C, H and OH, on both $(0001)_{\mathrm{Zr}}$ and $(0001)_{\mathrm{B}}$. These are presented as a radial distribution in the polar diagram of Fig. 2(a), where the binding strength of a particular adsorbent grows with the distance from the center of the diagram and the corresponding adsorption sites are marked along the rim.

The rank of the relative adsorption strength for the different atomic species involved is O ≥ C ≥ OH ≥ H on $(0001)_{\mathrm{Zr}}$ (O is the most strongly bonded species), which transforms into C ≥ O ≥ OH

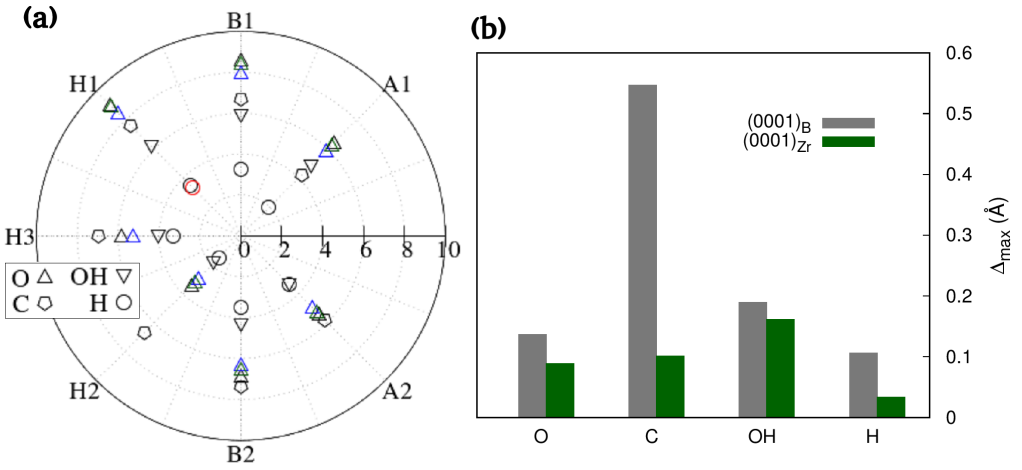

Figure 2: (a) Polar diagram of the adsorption energies, ΔE_{ads} (eV/atom), for the chemical species O, C, OH and H. Here H1, B1 and A1 (green shadow) are adsorption sites on $(0001)_{\mathrm{Zr}}$, and H2, H3, B2 and A2 (grey shadow) are on the $(0001)_{\mathrm{B}}$ surface. Our results in black are compared with those from Sayós's [10] in blue, Zhou's [12] in green and Xiao's [28] in red (note the latter two are shifted by half of the binding energies of O_2 and H_2, respectively). (b) The disturbance of the adsorbent surface, Δ_{max} (Å), are measured by the maximum displacement of the first atomic layer on the surface.

$\geq$ H on $(0001)_{\mathrm{B}}$ (C is the most strongly bonded species). In more detail we find for O the following ΔE_{ads}, 9.06, 3.44, 5.81, 8.59, 6.86, 6.43 and 5.42 (in eV/atom), respectively, at the sites **H1**, **H2**, **H3**, **B1**, **B2**, **A1** and **A2**. These values agree well with those from references [10, 12]. Furthermore, ΔE_{ads} for H is also in good agreement with that found by Xiao and coworkers [28]. Note that the ΔE_{ads} values extracted from Ref. [12] and Ref. [28] and reported in Fig. 2(a) are shifted by half of the binding energies of O_2 and H_2, respectively, due to the different reference states chosen in such works. At the same time in the case of the Zr (0001) surface we can only compare with results relative to metallic Zr [28], since those for ZrB_2 are not available in literature. To the best of our knowledge ΔE_{ads} information for C and OH on the $(0001)_{\mathrm{Zr}}$ and $(0001)_{\mathrm{B}}$ surfaces of ZrB_2 are reported here for the first time.

We find the hollow and bond-bridge sites to be energetically more favourable than the atop ones. This is generally true for both Zr- and B-terminated surfaces and for all the chemical species considered here. In fact, we compute ΔE_{ads} on the hollow and bond-bridge sites of the $(0001)_{\mathrm{Zr}}$ surface to range in the 3.22-9.06 eV/atom interval. These values are reduced to 1.52-7.39 eV/atom on the $(0001)_{\mathrm{B}}$ surface. In contrast, the A1/A2 atop sites are significantly less preferred, presenting even lower ΔE_{ads} values. The tendency of O to adsorbe preferentially on hollow and bond-bridge

sites has been validated by experiments [7] and other DFT-based calculations [10]. Here we extend the same information to C and OH.

Importantly, the chemical adsorption can induce a disturbance in the adsorbent surfaces. The maximum displacement of the outmost surface layer resulting from the adsorption, $\Delta_{\max}$ (Å), is computed and shown in Fig. 2(b). At variance with $\Delta E_{\rm ads}$, the $(0001)_{\rm B}$ surface atoms display $\Delta_{\max}$ values, for all the chemical species investigated, larger than those of $(0001)_{\rm Zr}$. We find that on $(0001)_{\rm Zr}$, the OH adsorbate causes the strongest disturbance, $\Delta_{\max} \sim 0.16$ Å; while on $(0001)_{\rm B}$, it is the C adatom to give the largest $\Delta_{\max}$ of 0.55 Å. This fact can be explained by the light weight of B and the strong chemical affinity between B and C (the existence of a stable B_4C compound with a melting point around 2800 K). In general, we find the $(0001)_{\rm B}$ surface to exhibit more prominent atomic disturbances than the $(0001)_{\rm Zr}$ counterpart.

In the following sections, we will discuss the adsorption mode of each molecule by examining the adsorption thermodynamics, the geometry of the adsorbate-adsorbent systems, the dissociation pathways and the associated activation energies. The adsorption and dissociation behaviour of the various molecules on B and Zr-terminated surfaces will also be compared.

4. Adsorption and dissociation of O_2

4.1. Adsorption mechanism

As a general feature our results indicate that molecular O_2 is prone to dissociative adsorption when laterally landing on the Zr- or B-terminated surfaces, but tends to adsorbe in the molecular form if vertically approaching. These two cases are distinguished by the filled and the open symbols in the polar diagrams of Fig. 3(a) and (b), where we present the different adsorption energies of O_2 over $(0001)_{\rm Zr}$ and $(0001)_{\rm B}$. The figure shows that all the dissociative adsorption starts from lateral geometries (left halves of the polar diagrams), while most of the molecular adsorption events originate from the vertical setups (right halves of the polar diagrams). Although dissociative adsorption of O_2 has been observed in experiments [5] in the past, the simple classification of the various adsorption mechanisms based on the surface-approaching geometry is suggested here for the first time.

As expected, the dissociated adsorption of O_2 is normally accompanied by a large variation of the O_2 geometry. In fact, the O-O interatomic length, l, of the dissociated O adatoms increases largely when compared to the equilibrium bond length of 1.48 Å, see Δ_l in Fig. 3(c), indicating the O-O bond breaking. The dissociated O adatoms then relax away from their initial adsorption location, and tend to finally adsorb on the hollow (**H**) and bond-bridge (**B**) sites. This agrees well

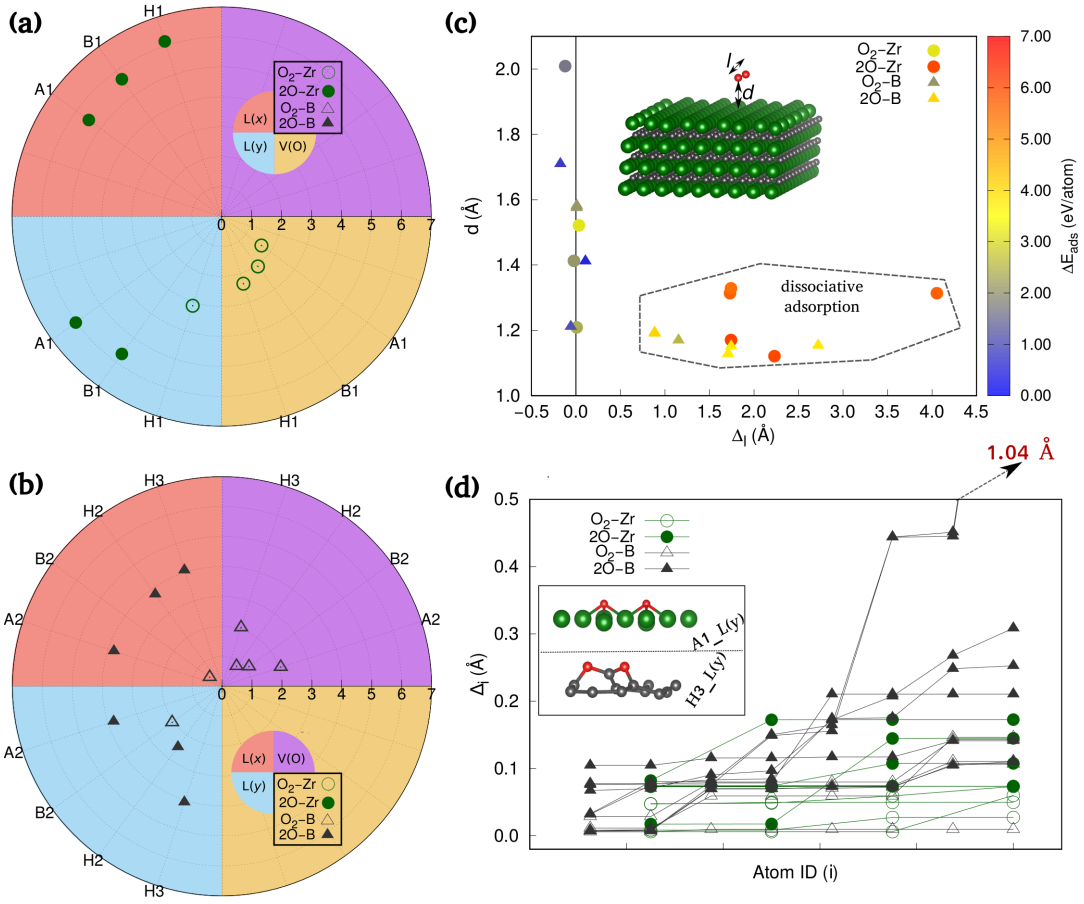

Figure 3: Adsorption energies (ΔE_{ads}, eV/atom) for O_2 on the (a) $(0001)_{\text{Zr}}$ and (b) $(0001)_{\text{B}}$ surfaces. Molecular (O_2) and dissociative (2O) adsorptions are distinguished by using open and filled symbols, respectively. The initial adsorption sites are marked along the rim of the polar diagrams, while the approaching geometries of the O_2 molecule are encoded as background color. These are further mapped as a function of the adsorption distance (d, Å) and the change in the interatomic length (Δ_l, Å) in panel (c). The definitions of d and l are shown in the inset (Δ_l is the change in l due to the adsorption). The distortion of the adsorbent surfaces (Δ_i) is plotted in panel (d) as a function of the surface atoms index (see inset and main text). (Color code: Zr = green spheres; B: grey spheres; O: red spheres).

with the energetic preference of the **H** and **B** sites discussed in section 3. Such behaviour has also been identified by Cheng et al. in Ref [13].

At the same time, the dissociative adsorption of O_2 results in strongly bonded O adatoms on the Zr-/B-surfaces, a feature clearly demonstrated by both the large adsorption energies, ΔE_{ads}, and the short adsorption distances, d; see Fig. 3(c). In fact, ΔE_{ads} for dissociative adsorption on the Zr (B)

surface is in the range 5.5-6.2 (2.5-4.1) eV/atom. These results can be compared with with values of 6.57-7.08 eV/atom, reported for ultra-soft-pseudopotential calculations at the GGA-PW91 level in Ref. [13] for dissociative adsorption of O_2 on Zr surface. In contrast, molecular adsorption of O_2 on the Zr-terminated (B-terminated) surface has a much lower $\Delta E_{\rm ads}$ range, 1.6-3.1 (0.5-2.1) eV/atom. The d values distribute within the narrow range of 1.1-1.3 (1.1-1.2) Å for dissociated adatoms on Zr (B) surface, bond lengths that are considerably shorter than those associated to molecular adsorbates (these can be as large as 2.0 Å). The strong chemisorption of the O adatoms on the ZrB_2 surfaces, with the corresponding large energy gain associated to the formation of the O-Zr and O-B bonds, makes dissociative adsorption thermo-dynamically more favorable than molecular adsorption.

An important feature to note is that dissociative adsorption comes with sometimes severe surface distortions or even surface reconstruction. In Fig. 3(d) the displacement of each surface atoms are plotted against their atom index. Dissociative adsorption of O_2 on $(0001)_{\rm Zr}$ activates surface reconstruction with an atomic displacement of 0.17 Åat the most. In contrast, dramatic effect is found for the **H3_L(y)** and **H3_L(x)** on $(0001)_{\rm B}$ adsorbate-adsorbent systems, which present displacements as large as 1.04 Å. In these cases the two O adatoms position themselves as first nearest neighours on the bond-bridge site after the O_2 dissociation. One B atom is then found to move above the original $(0001)_{\rm B}$ plane, thus breaking of the six-member ring symmetry of the $(0001)_{\rm B}$ surface; see the **H3_L(y)** illustration in the inset of Fig. 3(d). These results suggest that the dissociative adsorption of O_2 can trigger the reconstruction of the B-surface and therefore the easy formation of boron oxides. Note that the melting temperature of B_2O_3, the most common among the boron oxides, is only 723 K. This means that the formation of boron oxides during a high-temperature corrosion process will likely result in significant B mass loss.

4.2. Dissociation kinetics

When an O_2 molecule approaches the surface in a lateral configuration dissociative adsorption takes place without activation barrier, so that this is the most efficient reaction channel. However, in an O_2 gas one cannot exclude situations where the molecule attacks ZrB_2 with a vertical geometry. For this reason we have performed kinetic simulations for a number of candidate reactions involving both the vertical and lateral channel. For each one of them, the reactants (precursors) acting as the initial states are chosen from the adsorbed intermediates, while the dissociation products serving as the final states (FS) are selected among dissociated adatoms. More specifically, we explore the following O_2 reaction paths (paths labelled with 'a' are for reaction on the Zr-terminated surface,

while those with 'b' are for the B-terminated one):

$$\begin{cases} \mathbf{O_2 : H1\_V(O)} & \rightarrow & \mathbf{2O_{[ad,H1]}(1NN)} & \text{(a1)} \\ \mathbf{2O_{[ad,H1]}(1NN)} & \rightarrow & \mathbf{2O_{[ad,H1]}(2NN)} & \text{(a2)} \end{cases}$$

$$\begin{cases} \mathbf{O_2 : H2\_V(O)} & \rightarrow & \mathbf{O_2 : B2\_L(y)} & \text{(b1)} \\ \mathbf{O_2 : B2\_L(y)} & \rightarrow & \mathbf{2O_{[ad,B2]}(1NN)} & \text{(b2)} \\ \mathbf{2O_{[ad,B2]}(1NN)} & \rightarrow & \mathbf{2O_{[ad,B2]}(2NN)} & \text{(b3)} \end{cases}$$

When O_2 approaches the $(0001)_{Zr}$ surface with the vertical geometry **H1_V(O)**, it dissociates into two O adatoms after having tilted so to assume a lateral configuration [path (a1) of Fig. 4]. The so-produced O adatoms can occupy two adjacent hollow sites, thus forming a first nearest neighbour (1NN) pair, or they can diffuse further away from each other along the surface to take a second nearest-neighbour (2NN) position, as described by the (a2) path [see Fig. 4]. Both these paths are characterised by the absence of a kinetic barrier. However, if the O adatoms diffuse towards the atop sites (energetically less favorable than the hollow ones), an energy barrier of 0.59 eV is found. In Ref. [13] an activation barrier of 0.16 eV was determined for the vertical channel starting from the **A1** site. The dissociation path for vertical adsorption discussed here, namely the combination of paths (a1) and (a2), appears, however more energetically and kinetically advantageous.

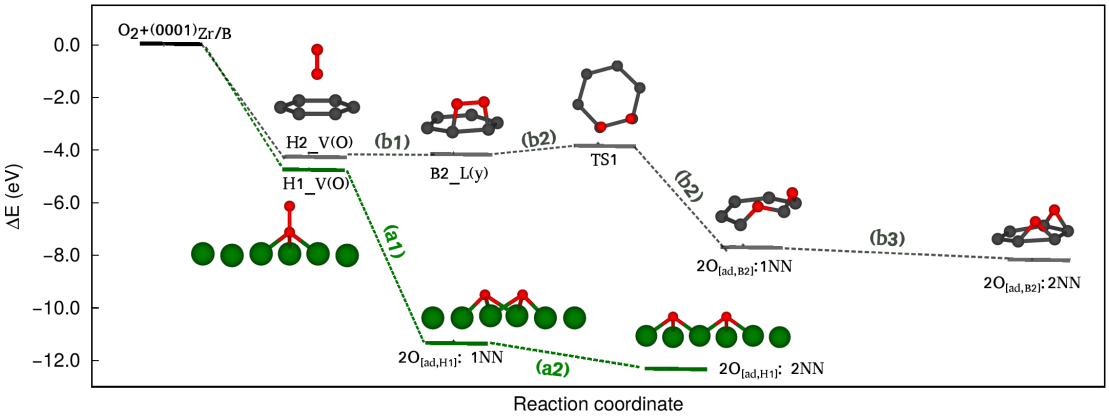

Figure 4: Dissociation paths of O_2 on the $(0001)_{Zr}$ surface via the (a1) and (a2) paths; and on the $(0001)_B$ one along the paths (b1), (b2) and (b3). In this second case one transition state (TS1), with energy barrier 0.38 eV, is observed. Colour code: Zr = green; B grey; O = red.

Turning now our attention to the dissociation of O_2 on $(0001)_B$, we note that this is weakly activated. The vertical configuration **H2_V(O)** can firstly rotate into the lateral **B2_L(y)**, as

illustrated by path (b1). Thereafter, the O_2 adsorbate dissociates into two O-adatoms located at the **B2** sites. This second step, path (b2), comes with a low activation barrier of 0.38 eV, a value in close agreement with the previously calculated one of 0.27 eV from Sayós et al. [10]. Then, the two O adatoms can occupy either the 2NN or the 1NN **B2** sites, by moving without energy barrier along path (b3). Notably, the 1NN **B2** adsorbate geometry promotes a strong distortion of the B surface by breaking the six-member B ring. For this reason the 2NN-**B2** configuration is more energetically and kinetically favorable.

5. Adsorption and dissociation of H_2O

5.1. Adsorption mechanism

In general we find that water exhibits the characteristics of chemisorption on the $(0001)_{Zr}$ surface, while physisorption dominates for the $(0001)_B$ one. In more detail, when a H_2O molecule approaches the $(0001)_{Zr}$ surface in a vertical position with the O atom closer to the surface, then the typical ΔE_{ads}'s are between 207 meV/atom and 368 meV/atom, as illustrated in Fig. 5(a). These values reduce by approximately a factor of four in situations where it is the hydrogen side of the molecule to form contact to the surface, and the ΔE_{ads} range is now 34-94 meV/atom. The only exception to this trend is for the **B1_V(H, x)** geometry for which we compute a ΔE_{ads} of 368 meV/atom. It must be noted that **B1_V(H, x)** is a highly symmetric structure, with the two protons taking the **H1** sites and the oxygen sitting on the **B1** site.

In contrast, if the H_2O molecule is adsorbed on $(0001)_B$, we will notice that both lateral and vertical configurations result in weakly bonded absorbates, with the ΔE_{ads}'s clustering around the 39-118 meV/atom interval. Only four configurations are observed with relatively large adsorption energies, all above 200 meV/atom. These are all initiated with the O atom placed over the **H3** site, but they consistently relax towards the **A2** one, a position that offers a more balanced adsorption configuration for both O and H.

Then we move to discuss the possibility of dissociative adsorption. This is observed on the $(0001)_{Zr}$ surface, although for significantly less configurations and with a much lower energy gain than what found for O_2. In fact, only the **H1_L(y)** configuration presents a clear evidence of dissociative adsorption with a ΔE_{ads} of 1.88 eV/atom; see Fig 5(a). In fact, in this case the final relaxed configuration shows an increase in the O-H bond length of more than 2.2 Å, while the bond angle decreases by about 50° [see the blue symbol in Fig. 5(c)]. No other approaching geometry of H_2O on $(0001)_{Zr}$ displays significant signs of molecular configuration change, with the bond lengths

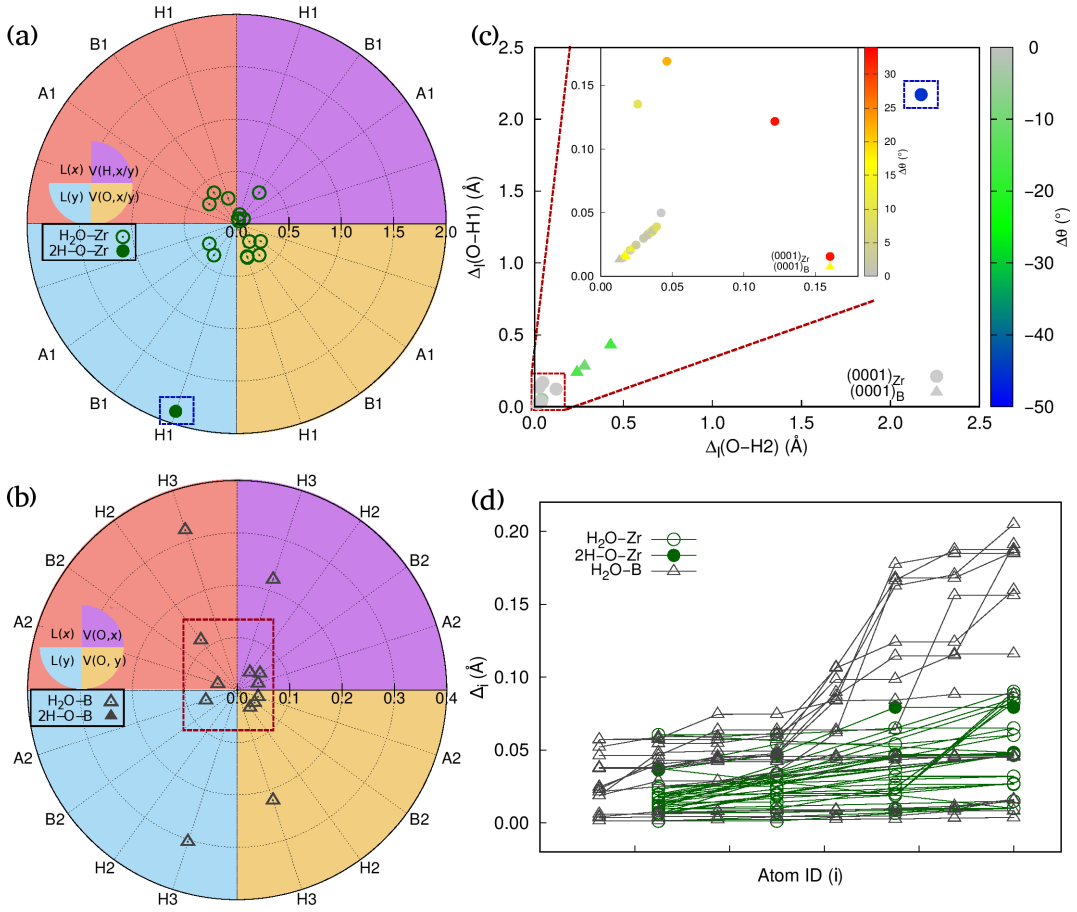

Figure 5: Adsorption energies, ΔE_{ads} (eV/atom), for H_2O on the (a) $(0001)_{\mathrm{Zr}}$ and (b) $(0001)_{\mathrm{B}}$ surfaces. Molecular (H_2O) and dissociative (2H-O) adsorptions are distinguished by using open and filled symbols, respectively. The adsorption sites are marked along the rim of the polar diagrams, while the approaching configurations of the H_2O molecules are encoded as background color. The distortion of the H_2O geometry is analysed in panel (c) where the deviation of one H-O bond length, Δ_l(O-H1), from its equilibrium value is plotted against the other, Δ_l(O-H2), and the color scale maps the change in bond angle, Δ_θ. The inset zooms in the mild-distortion region. The distortion of the adsorbent surfaces, Δ_i, is plotted in panel (d) as a function of the surface atoms index (see main text).

and bond angle remaining close to that of H_2O in the gas phase [see grey symbols in the inset of Fig. 5(c)]. A somewhat intermediate situation is found for H_2O attacking the $(0001)_{\mathrm{B}}$ surface. In this case, three lateral configurations, namely **H2_L(y)**, **B2_L(x)** and **B2_L(y)**, display significant bond-length expansion (0.2-0.5 Å) and bond angle contraction [green symbols in Fig. 5(c)]. These distortions, however, are not large enough to define the O-H bond breaking.

The disturbance of the surface atoms caused by the adsorption of H_2O is found to be minor

when compared to O_2 adsorption [see Fig. 5(d)]. In fact, we find that the maximum displacement of the surface atoms is always less that 0.21 Å, while it was 1.04 Å for O_2. This is consistent with the $\Delta E_{\rm ads}$'s for water being significantly smaller (in absolute value) than that of O_2. To summarise, our results indicate that H_2O adsorption is less active than O_2 adsorption, it is characterised by modest adsorption energies and small geometry distortions of both the molecule and the surface.

5.2. Dissociation kinetics

Given the more complex structure of H_2O with respect to that of O_2, its surface dissociation kinetic is also more complex. Here we consider the following potential reaction paths, where again 'a'-labelled paths are for $(0001)_{\rm Zr}$, while 'b'-labelled ones are for $(0001)_{\rm B}$.

$$\begin{cases} \mathbf{H_2O : B1\_V(O)} & \rightarrow \quad \mathbf{OH_{[ad,H1]} + H_{[ad,H1]}} & \text{(a1)} \\ \mathbf{OH_{[ad,H1]} + H_{[ad,H1]}} & \rightarrow \quad \mathbf{2H_{[ad,H1]} + O_{[ad,H1]}} & \text{(a2)} \end{cases}$$

$$\begin{cases} \mathbf{H_2O : B1\_V(O)} & \rightarrow \quad \mathbf{O_{[ad,B1]} + H_2(g)} & \text{(a3)} \end{cases}$$

$$\begin{cases} \mathbf{H_2O : A1\_L(y)} & \rightarrow \quad \mathbf{2H_{[ad,H1]} + O_{[ad,H1]}} & \text{(a4)} \end{cases}$$

$$\begin{cases} \mathbf{H_2O : A2\_L(y)} & \rightarrow \quad \mathbf{OH_{[ad,B2]} + H_{[ad,A2]}} & \text{(b1)} \\ \mathbf{OH_{[ad,B2]} + H_{[ad,A2]}} & \rightarrow \quad \mathbf{2H_{[ad,A2]} + O_{[ad,B2]}} & \text{(b2)} \end{cases}$$

$$\begin{cases} \mathbf{H_2O : A2\_L(y)} & \rightarrow \quad \mathbf{2H_{[ad,B2]} + O_{[ad,B2]}} & \text{(b3)} \end{cases}$$

On $(0001)_{\rm Zr}$, we primarily explore the dissociation of H_2O starting from **B1_V(O)**, an energetically preferred adsorbate geometry. Our results are illustrated in Fig. 6. When the molecule moves along the (a1) path, it tilts and rotates so to first lose one proton, thereby forming an intermediate state with the OH and H groups absorbed at two adjacent hollow sites. This intermediate state can further dissociate into a final one, in which H and O adatoms all sit at hollow sites. We denote this second channel as (a2). Two transition states, named TS1 and TS2, are detected for such combined (a1)+(a2) dissociation path, with energy barriers, $E_{\rm b}$, of 0.09 eV and 0.64 eV, respectively. In an alternative path, (a3), a H_2O molecule approaching with the **B1_V(O)** geometry directly dissociates into atomic O by releasing the two protons in the form of a H_2 gas molecule. The associated transition state, before H_2 release, has two protons separated by a distance of 1.09 Å, while the O atom is adsorbed on the surface at a distance of about 1.56 Å. The activation barrier for such path is, however, very high, 2.16 eV, making such a path available only at extremely elevated temperatures. Finally, a lateral channel initiated at the **A1_L(y)** structure can be activated by the expansion of the H-O-H bonds along path (a4). This is characterised by an energy barrier, at the TS4 transition

state, of 0.94 eV. Thus, we conclude that on $(0001)_{Zr}$ the (a1) path, with the low activation energy of 0.09 eV, is the most kinetically favourable and dominates the dissociation of H_2O into the OH and H groups. Notably, this is the same dissociation reaction experimentally observed for H_2O on ZrC(001) [9].

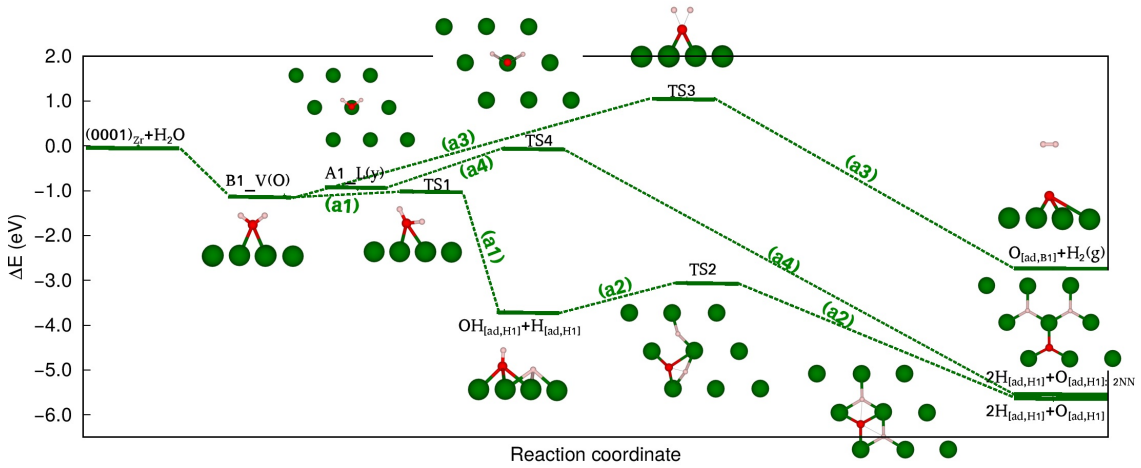

Figure 6: Dissociation of H_2O on the $(0001)_{Zr}$ surface. The initial states considered are **B1_V(O)** and **A1_L(y)**. Along the (a1)+(a2) path the reaction proceeds by first producing an OH group and a H atom and then by dissociating OH, so that the final state has two H and one O at adjacent hollow sites. Along path (a3) a H_2O molecule approaching as **B1_V(O)** releases an H_2 molecule, leaving an O atom on the surface. The vertical path (a4) also exhibits direct dissociation into two H and one O adatom, but these are placed at 2^{nd} nearest neighbors positions. Four transition states are determined with the following energy barriers, TS1: 0.09 eV, TS2: 0.65 eV, TS3: 2.16 eV, TS4: 0.94 eV. Colour code: Zr = green; O = red; H = pink.

Moving now to the $(0001)_B$ surface, the dissociation of H_2O is studied starting from the stable adsorbate geometry **A2_L(y)** along the two reaction paths illustrated in Fig. 7 [see also reaction path list]. When going along (b1)+(b2) there is a first dissociation into an OH group and a H atom, followed by the the decomposition of OH. The final dissociated geometry has O on the bond-bridge site and the two H on the atop ones. For this reaction there are two activation barriers of 0.44 eV and 0.91 eV, corresponding to a single deprotonation of H_2O and OH, respectively. The relatively high barrier for OH deprotonation, together with the fact that the energy of fully dissociated configuration is higher than the one in which the OH group remains intact on the surface, make this decomposition channel unlikely. In an alternative path, (b3), one O and two H adatoms are released simultaneously, ending up at three **B2** sites. A transition state, TS3, with an energy barrier of 1.10 eV is identified along this path. TS3 is characterised by the water molecule placed

with the O atom at the bond-bridge site and the two H ones moving toward the adjacent bridge positions (see Fig. 7) with elongated O-H bonds. As such, also for the $(0001)_{\mathrm{B}}$ surface we conclude that the dissociation of H_2O is likely to proceed by sequential single deprotonations.

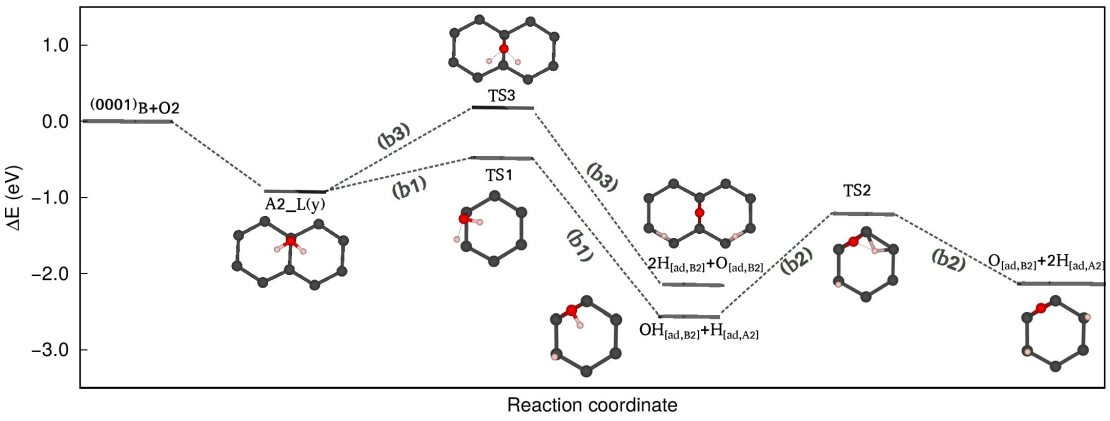

Figure 7: Dissociation of H_2O on the $(0001)_{\mathrm{B}}$ surface initiated at the **A2_L(y)** geometry. We identify two main reaction channels, one involving sequential single deprotonation, (b1)+(b2), and one associated to a double deprotonation, (b3). Three transition states are identified along these paths with the energy barriers, TS1: 0.44 eV, TS2: 0.91 eV, TS3: 1.10 eV. Colour code: B = grey; O = red; H = pink.

6. Adsorption and dissociation of CO

6.1. Adsorption mechanism

In this section we investigate the energetics of CO adsorption. In general, our calculations show that CO can be chemisorbed on both ZrB_2 surfaces with typical adsorption strengths falling in between those of O_2 and H_2O. In fact, we find ΔE_{ads}'s on the Zr-terminated (B-terminated) surface within the range 1.22-2.81 eV/atom (0.51-2.51 eV/atom), see Figs. 8(a) and 8(b).

On $(0001)_{\mathrm{Zr}}$ the lateral CO configurations are in general more energetically stable than the vertical ones, similarly to what found for O_2 and H_2O adsorption. It is worth mentioning that the initial geometries **H1_L(x)** and **B1_L(y)** can rotate into tilted structures and finally settle with O on the **B1** and C on the **H1** site. The top view of the final configuration of **H1_L(x)** is illustrated in the inset of Fig. 8(a). Note that the **B1** and **H1** adsorption sites are energetically rather similar, therefore in competition for adsorption.

In contrast, on $(0001)_{\mathrm{B}}$ it is the vertical adsorption to be more energetically favourable. Furthermore, we find that when CO is landing on the surface in a lateral configuration it can always rotate

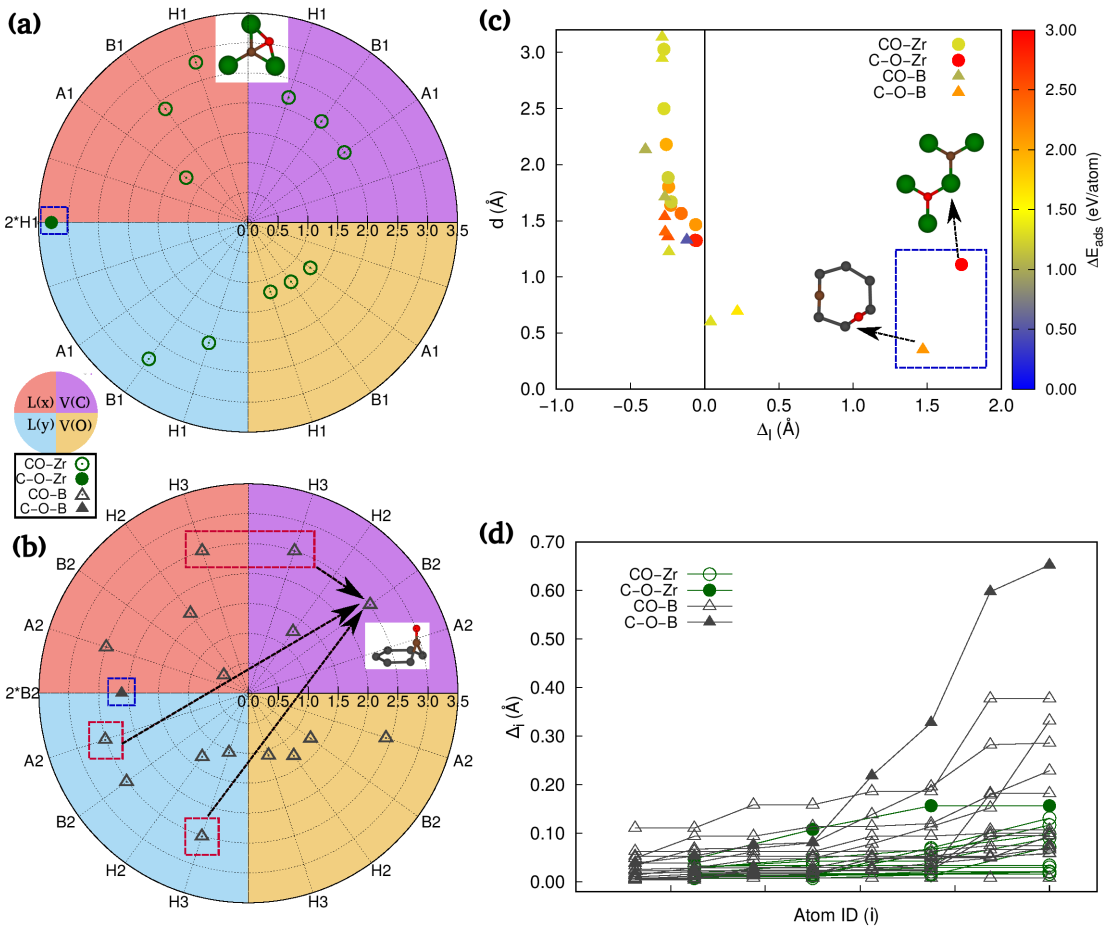

Figure 8: Adsorption energies, ΔE_{ads} (eV/atom), for CO on the (a) $(0001)_{\text{Zr}}$ and (b) $(0001)_{\text{B}}$ surfaces. Molecular (CO) and dissociative (C + O) adsorptions are distinguished by using open and filled symbols, respectively. The adsorption sites are marked along the rim of the polar diagrams, while the approaching configurations of the CO molecules are encoded as background color. The insets illustrate the preferred final configurations of the adsorbates. Note that on $(0001)_{\text{B}}$, **H3_L(x)**, **H3_L(y)** and **A2_L(y)** all transform into **B2_V(C)**, so that their corresponding ΔE_{ads} are the same (red dashed boxes). In panel (c) we map ΔE_{ads} as a function of the adsorption distance, d (Å), and the change in interatomic lengths, Δ_l (Å). The distortion of the adsorbent surfaces, Δ_i (Å), is plotted in panel (d) as a function of the surface atoms index (see main text). Colour code: Zr = green; B = grey; C = brown; O = red.

to assume a vertical structure during the geometry relaxation. For example, we find that **H3_L(x)**, **H3_L(y)** and **A2_L(y)** all transform into **B2_V(C)**. As such their adsorption energies, ΔE_{ads} turn out to be all the same, as highlighted by the red dashed boxes of Fig. 8(b), while their final adsorbate geometry is shown in the inset. In the same way, we find that the lateral configurations

H2_L(x) and **H2_L(y)** all relax into the tilted **H2_V(C)** one. We believe that such strong preference for vertical geometries is associated to the chemical affinity difference between C-B and O-B.

Importantly, for CO we do not find any evidence of direct dissociative adsorption on either $(0001)_{\mathrm{Zr}}$ or $(0001)_{\mathrm{B}}$, a fact that holds true for both lateral and vertical approaching geometries. The relative small variations in bond length of the various configurations are presented in Fig. 8(c). In order to complete our adsorption energy study we have also specifically constructed two dissociated configurations, namely $\mathbf{O_{[ad,H1]}}$-$\mathbf{C_{[ad,H1]}}$ and $\mathbf{O_{[ad,B2]}}$-$\mathbf{C_{[ad,B2]}}$, whose geometries are illustrated in the insets of Fig. 8(c). These present ΔE_{ads} values rather close to those found for molecular adsorbates, as it can be noted by comparing the empty and filledsymbols in Figs. 8(a) and 8(b). Such close energetics between molecular and dissociated adsorbates is indicative of a weak thermodynamic driving force to break the C-O bond during the surface adsorption.

Finally, the atomic distortions of the surface atoms due to the adsorption of CO are displayed in Fig. 8(d) as a function of the surface atom index. For molecular adsorption we find that B atoms move within the interval 0.004-0.38 Å, while the range for Zr is significantly more narrow, 0.008-0.13 Å. Large distortions are found only for dissociated configurations on the B-terminated surface, 0.65 Å, while they remain modest on the Zr-terminated one, 0.16 Å. Thus, we conclude that the surface distortions caused by CO is much less severe than that associated to O_2, but more pronounced than that of H_2O. This is consistent with the same ranking found for the adsorption energies. As such, there is compelling evidence that O_2 is the most active chemical molecule on ZrB_2 surfaces, followed by CO and lastly by H_2O.

6.2. Dissociation kinetics

Since molecular CO can be adsorbed both laterally and vertically on $(0001)_{\mathrm{Zr}}$, and only vertically on $(0001)_{\mathrm{B}}$, we decide to examine the following dissociation paths,

$$\begin{cases} \mathbf{CO:H1\_V(C)} & \rightarrow & \mathbf{CO:B1\_L(y)} & \text{(a1)} \\ \mathbf{CO:B1\_L(y)} & \rightarrow & \mathbf{C_{[ad,H1]}} + \mathbf{O_{[ad,H1]}} & \text{(a2)} \\ \mathbf{CO:B2\_V(C)} & \rightarrow & \mathbf{C_{[ad,B2]}} + \mathbf{O_{[ad,B2]}}(\mathbf{2NN}) & \text{(b1)} \end{cases}$$

On $(0001)_{\mathrm{Zr}}$ we start by taking **H1_V(C)** as initial CO geometry. This is thermodynamically less stable than the lateral configuration, **B1_L(y)**, and in fact our NEB calculation reveals that **H1_V(C)** can transform into **B1_L(y)** without any activation barrier [see path (a1) in Fig. 9]. Then, the lateral adsorbate **B1_L(y)** can decompose into two final adatoms, $\mathbf{C_{[ad,H1]}}$ and $\mathbf{O_{[ad,H1]}}$,

located at 2nd nearest-neighbour positions. The decomposition takes place along the (a2) path of Fig. 9. Along such reaction trajectory one encounters a transition state, TS1, where the two adatoms are in a 1st nearest-neighbour position. The transition state corresponds to the saddle point of the O migration and the associated activation barrier is 0.90 eV.

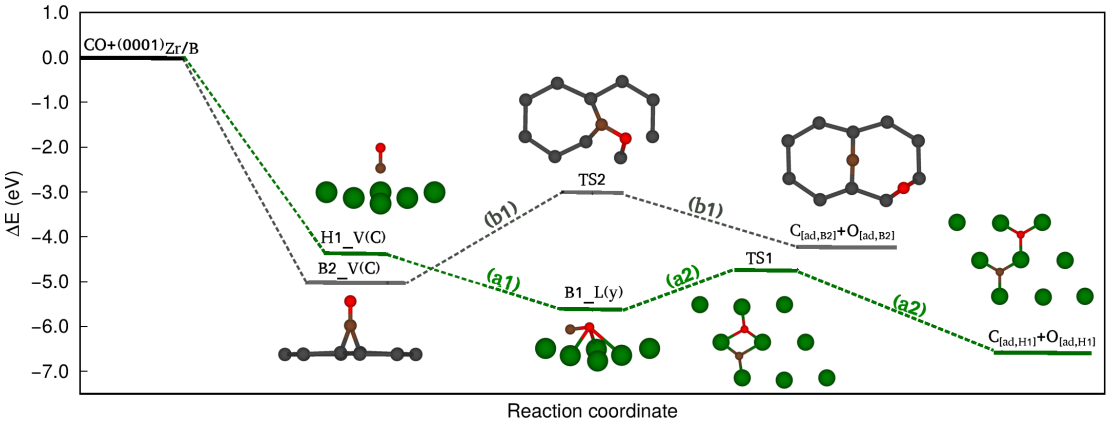

Figure 9: Dissociation of CO over $(0001)_{Zr}$ (green line) and $(0001)_B$ (grey line) along the paths (a1)+(a2) and (b1), respectively. Two transition states, TS1 and TS2, are identified respectively for $(0001)_{Zr}$ and $(0001)_B$ with energy barriers 0.90 eV and 2.01 eV. Colour code: Zr = green; B = grey; C = brown; O = red.

In contrast, on $(0001)_B$ the preferred adsorption geometry is vertical. In fact, any lateral configuration investigated rotates to a vertical position upon DFT relaxation, namely it cannot be stabilised even as metastable state. As representative configuration we then take **B2_V(C)**, which possesses the lowest adsorption energy on $(0001)_B$ [see (b1) channel in Fig. 9]. The final state considered is made of two adatoms, $\mathbf{C_{[ad,B2]}}$ and $\mathbf{O_{[ad,B2]}}$, occupying 2nd nearest-neighbour positions. Such reaction path contains a transition state, TS2, in which the B hexagonal structure is broken and the CO molecule effectively replaces on B atom. The activation barrier at the transition state is rather large, namely 2.01 eV.

As noted before, the chemical activity of CO is located in between that of O_2 (the most reactive species) and that of H_2O (the less reactive species), and it can result in surface reconstruction, similarly to the O_2 case. However, the dissociation kinetics of CO shows a behavior totally different from that of O_2. In fact bond breaking in O_2 can take place without kinetic activation, while that of CO demands an activation energy of 0.90 eV on $(0001)_{Zr}$ and 2.01 eV on $(0001)_B$. Therefore, we conclude that ZrB_2 oxidation can dominate at relatively low temperatures, while corrosion caused by CO requires elevated temperatures to be active.

7. Discussion

ZrB_2, a strongly bonded compound presenting alternating Zr and B atomic planes, is likely to present a grain structure dominated by $(0001)_{Zr}$ and $(0001)_B$ facets, which are also the most energetically stable open surfaces under a broad range of growth conditions. These surfaces undergo corrosive attack in the aggressive atmosphere, containing O_2, H_2O and CO, typical of real-life combustion in aerospace applications. Here we investigate the first steps in the corrosion process, namely we focus on the initial surface reactions involving molecular adsorption and dissociation. Our calculations confirm that $(0001)_{Zr}$ generally promotes strongly bound adsorption and weakly activated dissociation. Therefore, the transition-metal-terminated $(0001)_{Zr}$ surface is found to be more chemical active than its $(0001)_B$ counterpart. This is not a surprise given the high reactivity of early transition metals.

Turning our attention to the $(0001)_B$ surface, this is characterised by a substantial reconstruction upon both CO and O_2 dissociation. The limiting kinetic process in the first case is determined by a large activation barrier of 2.01 eV. In contrast, O_2 dissociation requires a much more modest activation energy, 0.38 eV, so that the formation of boron oxides is likely to be determined by the O_2 supply. The final reaction product, B_2O_3, has a relatively low melting point ($\sim$700 K), while evaporation takes place above 1500 K. Thus, we expect that at intermediate temperatures B layers can be easily depleted due to the presence of O_2, a mechanism similar to the C loss observed in ZrC [8]. This appears to be the most efficient mechanism for B depletion during combustion.

Furthermore, also at the $(0001)_{Zr}$ surface the dominant reaction is the dissociative adsorption of O_2, which proceeds spontaneously without activation. Importantly, the dissociated O adatoms can easily diffuse at the surface with migration paths presenting a barrier of 0.59 eV, but with the presence of barrier-less migration trajectories as well. When these results are combined together we can unambiguously suggest that the initial oxidation process of ZrB_2 can proceed rapidly. A possible strategy for limiting the corrosion may then be that of inserting additives into the ZrB_2 matrix. Alternatively one can develop appropriate surface treatments, such as pre-oxidation. This may form a protective ZrO_2 layer over ZrB_2. Importantly, ZrO_2 has high thermal stability (melting temperature, $T_m \leq 2900$ K), and the interface attachment between ZrB_2 and ZrO_2 can be controlled by controlling the ZrO_2 polymorphism.

8. Conclusion

In this work, we have presented a thorough atomistic modelling of the adsorption and dissociation of O_2, H_2O and CO over two of the most stable ZrB_2 surfaces. Several conclusions can be drawn from our results. Firstly, all the chemical species investigated, namely O, C, OH and H, display strong chemisorption on ZrB_2, with O and C showing the largest adsorption energies. In general, the preferred adsorption sites on both Zr- and B-terminated surfaces are the hollow and bridge ones. Secondly, we have found that O_2 dissociative adsorption prevails when the molecule laterally approaches the surface, while molecular adsorption dominates for vertical geometries. The same trend is also found for the other molecules, with the exception of CO on $(0001)_B$. Thirdly, we have determined that the chemical activity of the various adsorbents follows the ranking: O_2, CO and H_2O, with O_2 being the most active agent. H_2O is the less reactive of the molecules studies and tends to be chemisorbed on $(0001)_{Zr}$ and physisorbed on $(0001)_B$. The kinetic barriers for dissociation are instead ordered as O_2, H_2O and CO, with CO presenting anactivation barrier of 0.90 eV on $(0001)_{Zr}$ and of 2.01 eV on $(0001)_B$. This makes O_2 the most aggressive chemical agent for ZrB_2. Finally, we have determined that the Zr-surface is chemically more active than the B-terminated one, at least to the chemical agents studied here. Considering the low melting point of the B-containing products, the B-surfaces are likely to be destroyed under O_2 and/or CO attack, a mechanism likely to determine B mass lost during combustion.

As it stands, our work offers a complete view of the microscopic mechanism for reaction of O_2, CO and H_2O on ZrB_2 surfaces. This is important to determine the first steps in the corrosion process. Future work on the effects of the intermediate products and of the temperature is necessary for defining a complete picture of oxidation and corrosion in UHTC materials.

Acknowledgement

This research was supported by the European Union's Horizon 2020 "Research and innovation programme" under the grant agreement No.685594 (C^3HARME). Computational resources have been provided by the Irish Center for High-End Computing (ICHEC) and the Trinity Centre for High Performance Computing (TCHPC). Y.Z. would like to thank the support from the internal grant of Yanshan University and the 100 Talents Programme of Hebei province.

Reference

References

[1] Padture, N. P. *Nature Materials* **2016**, *15*, 804–809.

[2] Zeng, Y.; Wang, D.; Xiong, X.; Zhang, X.; Withers, P. J.; Sun, W.; Smith, M.; Bai, M.; Xiao, P. *Nature Communications* **2017**, *8*, 15836.

[3] Fahrenholtz, W. G.; Hilmas, G. E. *Scripta Materialia* **2017**, *129*, 94–99.

[4] Cahill, J. T.; Turner, S.; Ye, J.; Shevitski, B.; Aloni, S.; Baumann, T. F.; Zettl, A.; Kuntz, J. D.; Worsley, M. A. *Chemistry of Materials* **2019**, *31*, 3700–3704.

[5] Aizawa, T.; Hayami, W.; Otani, S. *Journal of Chemical Physics* **2002**, *117*, 11310–11314.

[6] Belyansky, M.; Trenary, M. *Inorganica Chimica Acta* **1999**, *289*, 191–197.

[7] Hayami, W.; Souda, R.; Aizawa, T.; Tanaka, T.; Ishizawa, Y. *JJAP series* **1994**, *10*, 172–173.

[8] Kato, S.; Ozawa, K.-i.; Edamoto, K.; Otani, S. *Japanese Journal of Applied Physics* **2000**, *39*, 5217–5222.

[9] Kitaoka, H.; Ozawa, K.; Edamoto, K.; Otani, S. *Solid State Communications* **2001**, *118*, 23–26.

[10] Gamallo, P.; Sayós, R. *Journal of Physical Chemistry C* **2013**, *117*, 5831–5839.

[11] Sun, W.; Dai, F.; Xiang, H.; Liu, J.; Zhou, Y. *Journal of Materials Science and Technology* **2019**, *35*, 584–590.

[12] Sun, W.; Liu, J.; Xiang, H.; Zhou, Y.; Sinnott, S. *Journal of the American Ceramic Society* **2016**, *99*, 4113–4120.

[13] Cheng, C.; Li, H.; Fu, Q. *Computational Materials Science* **2018**, *153*, 282–287.

[14] Valdés, H.; Molina, L. M.; Alonso, J. A. *Applied Surface Science* **2019**, *487*, 244–252.

[15] Osei-Agyemang, E.; Paul, J. F.; Lucas, R.; Foucaud, S.; Cristol, S. *Journal of Physical Chemistry C* **2014**, *118*, 12952–12961.

[16] Fahrenholtz, W. G.; Hilmas, G. E.; Talmy, I. G.; Zaykoski, J. A. *Journal of the American Ceramic Society* **2007**, *90*, 1347–1364.

[17] Aizawa, T.; Suehara, S.; Hishita, S.; Otani, S. *Journal of Physics: Condensed Matter* **2008**, *20*, 265006.

[18] Suehara, S.; Aizawa, T.; Sasaki, T. *Physical Review B* **2010**, *81*, 85423.

[19] Zhang, Y.; Sanvito, S. *Journal of American Ceramic Society* **2018**, *101*, 4118–4127.

[20] Blöchl, P. E. *Physical Review B* **1994**, *50*, 17953–17979.

[21] Kresse, G.; Joubert, D. *Physical Review B* **1999**, *59*, 1758–1775.

[22] Perdew, J. P.; Burke, K.; Ernzerhof, M. *Physical Review Letters* **1996**, *77*, 3865–3868.

[23] Saqlain, M. A.; Hussain, A.; Siddiq, M.; Leitão, A. A. *Applied Surface Science* **2018**, *435*, 1168–1173.

[24] Grimme., S. *Journal of Computational Chemistry* **2006**, *27*, 1787–1799.

[25] Makov, G.; Payne, M. C. *Physical Review B* **1995**, *51*, 4014–4022.

[26] Henkelman, G.; Uberuaga, B. P.; Jonsson, H. *Journal Of Chemical Physics* **2000**, *113*, 9901–9904.

[27] Henkelman, G.; Jonsson, H. *Journal Of Chemical Physics* **2000**, *113*, 9978–9985.

[28] Zeng, C.; Wang, B.; Wang, L.; Li, Y.; Nie, Y.; Xiao, W. *Nuclear Materials and Energy* **2017**, *13*, 28–34.